Ring Structures by Coagulation of Dust Aggregates in Protostellar Disks observed by ngVLA

Satoshi Ohashi, [1] Hiroshi Kobayashi, [2] Nami Sakai [1]
[1] *RIKEN Cluster for Pioneering Research, 2-1, Hirosawa, Wako-shi, Saitama 351-0198*
satoshi.ohashi@riken.jp
[2] *Department of Physics, Graduate School of Science, Nagoya University, Furo-cho, Chikusa-ku, Nagoya 464-8602*

Abstract

We study coagulation of dust aggregates in a Keplerian rotating disk to investigate the grain growth, leading to the planet formation. By calculating the evolution of dust surface density and dust size, we find that the dust grains grow in an inside-out manner because the growth timescale is roughly proportional to the orbital period. The boundary of the dust evolution can be regarded as a growth front because large dust grains are formed inside the boundary, while the grain growth does not occur yet outside of the boundary. Radiative transfer calculations show that the growth front can be identified as a ring structure, and the spectral index will be one of the reliable observing ways to identify the growth front. We discuss that the ngVLA together with ALMA will allow us to reveal substructures in protostellar disks and testify the growth front model.

Key words: Circumstellar dust$_1$ — Protostellar disks$_2$ – Protoplanetary disks$_3$ – Planet formation$_4$

1. Introduction

The understanding of the planet formation is one of the major studies in astronomy because planets are ubiquitous in the universe. More than four thousands exoplanets have been discovered since the first discovery in 1995 (Mayor & Queloz 1995). Planets are known to be formed in circumstellar disks of gas and dust around young stars (Williams & Cieza 2011). Therefore, dust grains are thought to be building blocks for planets.

The planet formation can be regarded as size evolution of the dust grains from the typical size of $0.1-1$ μm in Inter Stellar Medium (ISM) to km-size of planetesimals. It is suggested that the dust grains are grown by sticking together and form the planetesimals in protoplanetary disks. However, the grain growth process is poorly understood because there are several issues for the planet formation. For example, the dust grains move radially inward due to the drag of the gas and cannot survive for the planet formation, which is called "radial drift barrier" (Adachi et al. 1976; Weidenschilling 1977). One of the other issues is "mass budget problem", which is that the dust in Class II protoplanetary disks may not be enough to explain the averaged solid mass in exoplanets (Andrews & Williams 2005; Andrews & Williams 2007).

Early stage of the disk evolution around Class 0/I protostars is one of the key targets to investigate the grain size evolution in the circumstellar disks. A survey of protostellar disks in the Orion molecular clouds showed that the protostellar dust disk masses are systematically larger than those of Class II disks by a factor of >4 (Tobin et al. 2020). Because the decrease in dust disk masses is expected from disk evolution by accretion, the grain growth may need to begin during the protostellar phase.

Recent high spatial resolution observations of millimeter and sub-millimeter wavelengths with interferometers such as the Atacama Large Millimeter/ submillimeter Array (ALMA) and the Very Large Array (VLA) reveal a variety of pictures of disk structures from the early stage of the disk formation (Takakuwa et al. 2017; Sheehan & Eisner 2017; Sheehan & Eisner 2018; Sai et al. 2020; Tobin et al. 2020; Garufi et al. 2020) to the late stage of protoplanetary disks (van der Marel et al. 2013; Casassus et al. 2013; ALMA Partnership et al. 2015; Isella et al. 2016; Andrews et al. 2018; Fedele et al. 2018; Tsukagoshi et al. 2019). In particular, dust ring structures have been observed in many protoplanetary disks. For example, the first ALMA Long Baseline Campaign observations show the prominent ring and gap structures of the HL Tau disk at 30 mas resolution (ALMA Partnership et al. 2015). The Disk Substructures at High Angular Resolution Project (DSHARP) project in the ALMA Cycle 4 Large program (Andrews et al. 2018) has also shown that disks have gap/ring structures in the sample of large and bright disks (Huang et al. 2018).

Interestingly, the dust ring structures are observed not only in class II protoplanetary disks, but also even in the earlier stages of disk formation around class 0 and class I objects (Sheehan & Eisner 2017; Sheehan & Eisner 2018; Sheehan et al. 2020; Nakatani et al. 2020; Segura-Cox et al. 2020). The formation of the ring structures in growing young disks are studied by Ohashi et al. (2020). They suggest that the growth front by coagulation of the dust grains can be observed as the ring structure because the disk has the radial distribution of the grain size and dust surface density. Ohashi et al. (2020) propose that the grain growth already begin in the protostellar disks.

The next-generation Very Large Array (ngVLA) offers high angular resolution ($\sim$10 mas) at long wavelengths ($17-93$ GHz or $3-18$ mm), which is sensitive to thermal emission from dust grains with a size of millimeter to centimeter. Thanks to its high sensitivity and high spatial resolution with the long wavelengths, ngVLA observations allow us to investigate the grain sizes in the protostellar disks with optically thin regime. In this paper, we show the idea of the growth front model and how the growth front is observed with (sub) millimeter wavelengths. We also show the current observational problem with ALMA and discuss the future solutions with ngVLA.

2. Ring Structure by Growth Front

2.1. Model

In this subsection, we describe a brief summary of dust coagulation model. Detail calculations are shown by Ohashi et al. (2020).

The dust evolution considers two conditions: (1) the dust grains grow via coagulation and (2) the dust grains have radial drift due to decouple from the gas motion.

The mass distribution of dust particles is assumed to have a single peak in mass $m_{\rm p}(r)$ at each radial distance r. Then, assuming that the dust surface density $\Sigma_{\rm d}$ at each orbit r is dominated by particles with mass $m_{\rm p}$, we follow how the peaks of dust surface density $\Sigma_{\rm d}$ and mass $m_{\rm p}$ change with coagulation and radial drift. According to Sato et al. (2016), the equations of the evolution of $\Sigma_{\rm d}$ and $m_{\rm p}$ are given by

$$\frac{\partial \Sigma_{\rm d}}{\partial t} + \frac{1}{r}\frac{\partial}{\partial r}(r v_{\rm r} \Sigma_{\rm d}) = 0, \tag{1}$$

$$\frac{\partial m_{\rm p}}{\partial t} + v_{\rm r}\frac{\partial m_{\rm p}}{\partial r} = \frac{2\sqrt{\pi} a^2 \Delta v_{\rm pp}}{h_{\rm d}}\Sigma_{\rm d}, \tag{2}$$

where $a = (3m_{\rm p}/4\pi\rho_{\rm int})^{1/3}$ is the particle radius, $v_{\rm r}$ is the radial drift velocity of the particles, $\Delta v_{\rm pp}$ is the relative velocity of the particles, $\rho_{\rm int}$ is the internal density of dust grains, and $h_{\rm d}$ is the dust scale height. The internal density of dust grains is fixed to be a typical value of $\rho_{\rm int} = 1.4$ g cm^{-3} for simplicity.

The initial gas surface density ($\Sigma_{\rm g}$) is set to be

$$\Sigma_{\rm g} = 1.7\times 10^3 \left(\frac{r}{1\ {\rm AU}}\right)^{-3/2} {\rm g\ cm^{-2}}, \tag{3}$$

based on the minimum mass solar nebula (MMSN) model of Hayashi (1981). The jump of the surface density across the snow line is ignored in this calculation because the snow line position of ~ 3 au is much smaller than the area to be investigated ($\sim 10-100$ au). The dust surface density ($\Sigma_{\rm d}$) is initiallly set to be 1% of the gas surface density.

The dust temperature is determined by a thermal equilibrium as follows

$$T = 280\left(\frac{r}{1\ {\rm AU}}\right)^{-1/2}\left(\frac{L}{L_\odot}\right)^{1/4} {\rm K}. \tag{4}$$

The initial size of the dust particle is uniformly set to 0.1 μm.

2.2. Dust Evolution

The global evolution of the dust surface density $\Sigma_{\rm d}$ and particle size a of the coagulation model is shown in Figure 1 . In this figure, the critical radius where the surface density remains the initial state on the outside, can be identified. Furthermore, this position moves outwards over time. This position can be considered as a growth front, where the dust evolution proceeds. For example, the growth front corresponds to ~ 10 au and ~ 24 au, at $t = 6.4\times 10^3$ yr and $t = 2.6\times 10^4$ yr, respectively. Importantly, we point out that the position of the growth front (the pebble production line) is independent of the dust structures, disk mass, temperature, or the turbulence strength as explained in the following discussion.

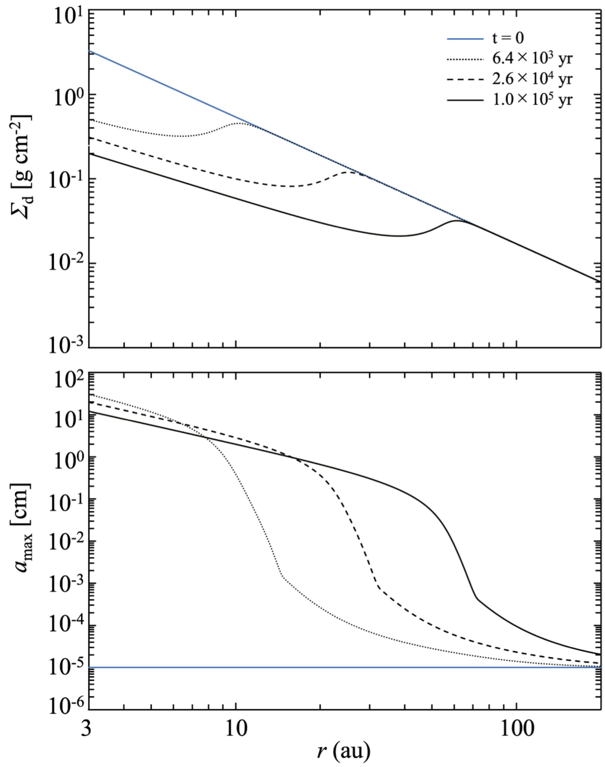

Fig. 1. Time evolution of the surface density Σ_d (*top panel*) and radius a (*bottom panel*) of dust particles as a function of orbital radius r for models with $a = 10^{-3}$. The blue lines show the initial conditions, while the black dotted, dashed, and solid lines are the snapshots at times $t = 6.4\times10^3$, 2.6×10^4, and 1.0×10^5 yr, respectively.

The dust evolution can be estimated from growth timescale (Takeuchi & Lin 2005; Garaud 2007; Brauer et al. 2008; Birnstiel et al. 2010; Birnstiel et al. 2012; Okuzumi et al. 2012, e.g.,). The growth rate of the aggregate mass m at the midplane is given by Tanaka et al. (2005) as

$$\frac{dm}{dt} = \rho_{\rm d}\sigma_{\rm col}\Delta v = \frac{\Sigma_{\rm d}\sigma_{\rm col}\Delta v}{\sqrt{2\pi}h_{\rm d}}, \tag{5}$$

where $\rho_{\rm d} = \Sigma_{\rm d}/(\sqrt{2\pi}h_{\rm d})$ is the spatial dust density at the midplane, $\sigma_{\rm col}$ is the collisional cross section of two dust particles. Then, Equation (5) can be rewritten in terms of the growth timescale as

$$t_{\rm grow} = \left(\frac{m}{\dot{m}}\right) = \frac{m\sqrt{2\pi}h_{\rm d}}{\Sigma_{\rm d}\sigma_{\rm col}\Delta v} = \frac{4\sqrt{2\pi}}{3}\frac{h_{\rm d}}{\Delta v}\frac{\rho_{\rm int}a}{\Sigma_{\rm d}}, \tag{6}$$

where $m = (4\pi/3)\rho_{\rm int}a^3$ and $\sigma_{\rm col} = \pi a^2$.

Here, we focus on the millimeter sized dust grains because these grains are sensitive to millimeter-wave emission. For millimeter-sized dust grains, $h_{\rm d} \sim \sqrt{\alpha_{\rm D}/{\rm St}}h_{\rm g}$ and $\Delta v \sim \Delta v_{\rm t} \sim \sqrt{\alpha_{\rm D}{\rm St}}c_{\rm s}$ (Brauer et al. 2008). Then, we obtain

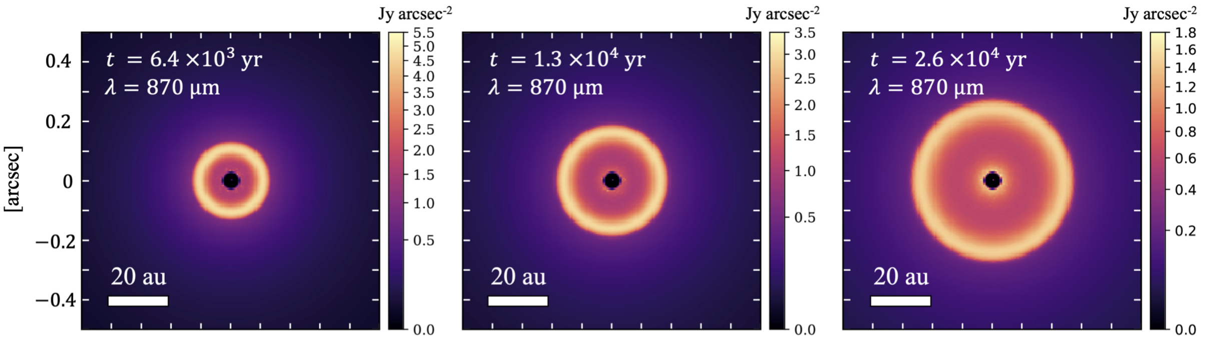

Fig. 2. The intensity maps of the dust coagulation model at $t = 6.4 \times 10^3$ yr, 1.3×10^4 yr, and 2.6×10^4 yr obtained by the radiative transfer calculations with RADMC-3D. The observing wavelengths are $\lambda = 870$ μm. The distance is 100 pc.

$$t_{\rm grow} \sim \left(\frac{\Sigma_{\rm g}}{\Sigma_{\rm d}}\right)\frac{1}{\Omega_{\rm K}}. \tag{7}$$

Equation (7) indicates that the dust evolution commences from inside out because the growth timescale is roughly proportional to the orbital period. Importantly, the growth time scale is independent on the other parameters such as the internal density of dust grains ($\rho_{\rm int}$) and turbulence ($\alpha_{\rm D}$) excepting for the dust to gas mass ratio ($\Sigma_{\rm g}/\Sigma_{\rm d}$). Therefore, the dust growth time is not affected by the fluffiness of dust, the disk mass, temperature, or the strength of the disk turbulence, while it becomes faster by increasing the dust mass ratio. Outside of the growth front, the dust particles still remain the initial state since the dust evolution is not proceeded yet, while the dust grains are grown inside of the growth front. As a result, the dust surface density is maximized in the growth front (see Figure 1). Therefore, a ring structure is expected to be observed at the growth front.

2.3. *Growth Front Location*

Based on the dust evolution, the radiative transfer calculations are performed by using RADMC-3D (Dullemond et al. 2012). The observing wavelength is set to 0.87 mm, which corresponds to ALMA band 7 observations.

Figure 2 shows images of the radiative transfer calculations of the model at $t = 6.4 \times 10^3$ yr, $t = 1.3 \times 10^4$ yr, and $t = 2.6 \times 10^4$ yr. The ring structure can be observed at the growth front and the position moves outward over time.

The ring location can be formulated since the growth front is roughly proportional to the orbital period. Equation (7) indicates the timescale of the dust evolution which is a function of the Keplerian frequency $\Omega_{\rm K}$. In other words, if the timescale ($t_{\rm grow}$) is set to the disk age ($t_{\rm age}$), we can derive the critical radius ($R_{\rm c}$) where the growth front reaches because $\Omega_{\rm K} \propto r^{-3/2}$. The critical radius can be estimated by transforming the equation (7) into a function of r. Thus, Equation (7) yields

$$R_{\rm c} = A\left(\frac{M_\star}{M_\odot}\right)^{1/3}\left(\frac{\zeta_{\rm d}}{0.01}\right)^{2/3}\left(\frac{t_{\rm disk}}{1\ {\rm yr}}\right)^{2/3} {\rm au} \tag{8}$$

where A is the transformation coefficient and $\zeta_{\rm d} = \Sigma_{\rm d}/\Sigma_{\rm g}$. The coefficient A can be derived by fitting the various ring positions in time to Equation (8). Therefore, we perform the radiative transfer calculations for the model at $t = 6.4 \times 10^3$ yr, 1.3×10^4 yr, 2.6×10^4 yr, 5.2×10^4 yr, and 1.0×10^5 yr by assuming $\lambda = 870$ μm, $M_\star = 1 M_\odot$, and $\zeta_{\rm d} = 0.01$. Then, we identify the ring position. Figure 3 shows the time evolution of the ring position. The error of the ring position indicates the full width half maximum (FWHM) derived by the direct measurements of the synthetic images. By fitting the ring positions to equation (8), A is derived to be 0.026.

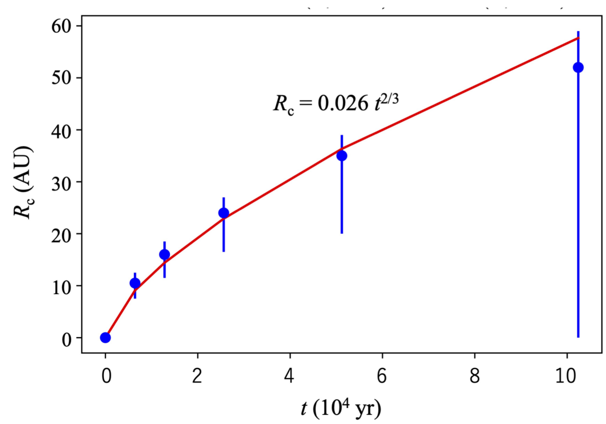

Fig. 3. The ring positions of our model against time. The red line indicates the fitting to equation (8) to derive the transformation coefficient A.

3. Observational Study of the Growth Front with ngVLA

We discuss the growth front and observations for the dust ring structures. As shown by Ohashi et al. (2020), the growth front location is consistent with the observed ring positions of the Class 0/I sources.

3.1. *Spectral Index Distributions*

The important evidence of the growth front would be the transition of the dust grain size across the growth front. Inside the growth front, dust grains as large as millimeter or centimeter size are formed because the grain growth proceeds. On the other hand, outside the growth front, small dust grains (~ 1 μm size) are still remained.

The spectral index will be one of the reliable ways to investigate the dust grain size distribution. Based on the dust evolution model and radiative transfer calculations, we derive the

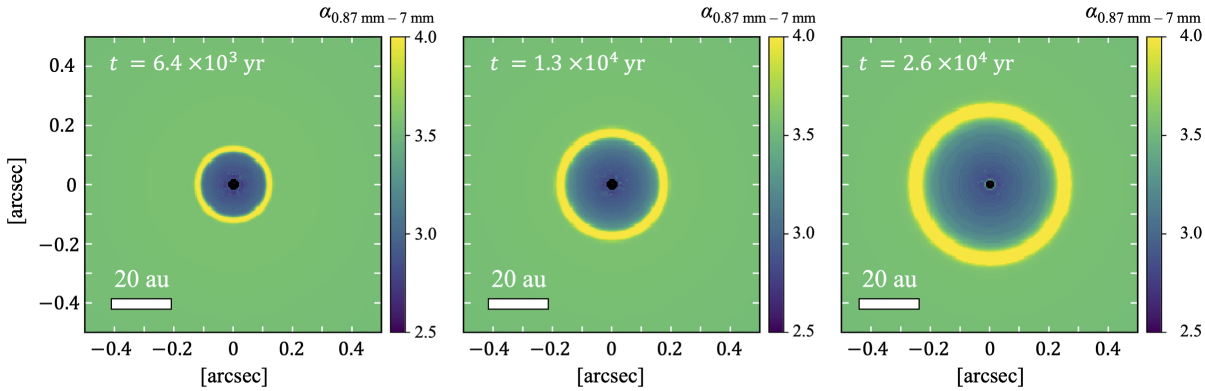

Fig. 4. The spectral index (α) maps of the dust coagulation model at $t = 6.4 \times 10^3$ yr, 1.3×10^4 yr, and 2.6×10^4 yr. The spectral index α is derived by the intensities of the 870 μm and 7 mm images.

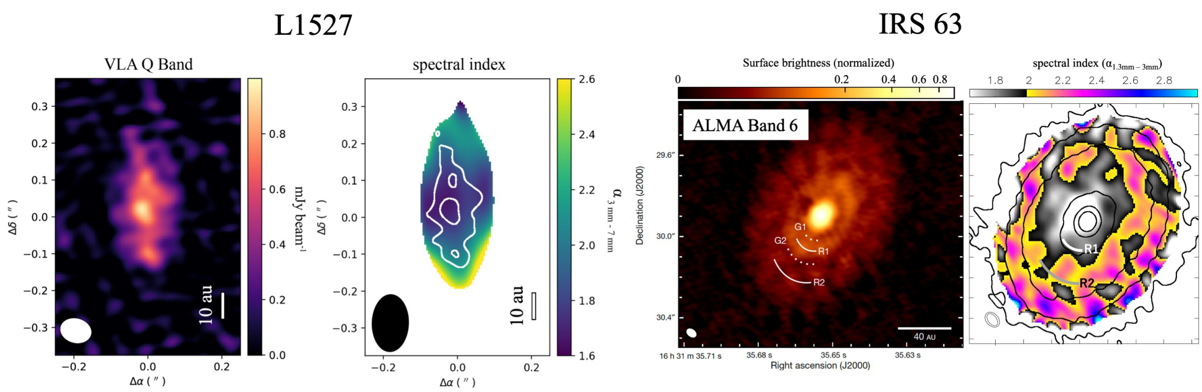

Fig. 5. (Left two panels) the VLA 7 mm dust continuum image and the spectral index map of L1527 (Nakatani et al. 2020; Ohashi et al. 2020). The spectral index is derived by the intensities between 3 mm and 7 mm wavelengths. (Right two panels) the ALMA 1.3 mm dust continuum image and the spectral index map of IRS 63 (Segura-Cox et al. 2020). The ring positions are shown in the white lines. The spectral index map is derived by the ALMA 1.3 mm and 3 mm dust continuum emission.

spectral index between 0.87 mm and 7 mm observing wavelengths. As shown in Figure 4, the growth front model predicts that the spectral index will change across the growth front. Therefore, observations of dust continuum emission with multiple wavelengths allow us to identify the evidence of the growth front for the ring formation mechanism in the protostellar disks.

3.2. *A Case Study of the Growth Front: L1527 and IRS 63*

We study the protostellar disks around L1527 and IRS 63 by using ALMA and VLA archival data. These disks have a ring (L1527) or multiple ring structures (IRS 63), and these ring positions are consistent with the growth front (Ohashi et al. 2021). By using 0.87 mm and 7 mm dust continuum emission for L1527, and using 1.3 mm and 3 mm dust continuum emission for IRS 63, we derive the spectral index distributions.

Figure 5 shows the spectral index maps of the L1527 and IRS 63 disks. The both disks show that the spectral index have $\alpha < 2$ nearby the protostars, and that seems to increase to $\alpha \sim 2.3$ in the outer regions. Even though the increasing trend of the spectral index with outer radii is consistent with the growth front model, the observed spectral indices of $\alpha \sim 1.6 - 2.3$ are much lower than the predictions of $\alpha \sim 2.6 - 3.7$ by the growth front model.

The discrepancy of the observations and model may be caused by high optical depth of the submillimeter dust continuum emission. If the emission becomes optically thick, it follows the black body radiation. Then, the spectral index is $\alpha = 2$ regardless of the grain size. In this case, the spectral index does not imply the grain size. By taking into account the beam dilution of the observations for these disks, the spectral indices can be larger than 2 but lower than that of the optically thin case.

We also point out that these disks have anomalously low (i.e., < 2.0) spectral indices nearby the protostars. Such low millimeter spectral indices can be achieved by optically thick emission with temperature gradients. Short wavelengths tend to be optically thicker and are opaque at the outer region of the disks. By taking into account the temperature gradient of the disk, the shorter wavelengths observe the outer cold regions. Thus, the spectral indices can be low values (i.e., < 2.0).

The self-scattering of dust grains (Kataoka et al. 2015) may also affect the intensity of the dust thermal emission and spectral index at millimeter wavelengths (Soon et al. 2017; Ueda et al. 2020). Liu (2019) and Zhu et al. (2019) pointed out that the spectral index decreases lower than 2 due to the scattering ef-

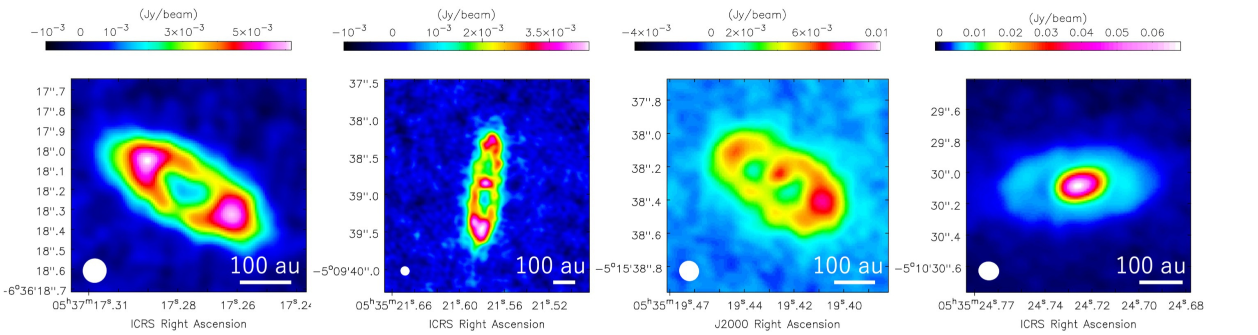

Fig. 6. Example images from ALMA 0.87 mm dust continuum observations toward selected protostellar disks having ring structures. The data is obtained by the VANDAM survey (Tobin et al. 2020). The synthesized beams are drawn in the lower left corner; the typical ALMA synthesized beam is 0 1 arcsec.

fect because the scattering of (sub)millimeter-sized dust grains makes the (sub)millimeter thermal emission fainter for optically thick emission. As a result, the spectral index becomes flatter or steeper than the case without scattering effect.

3.3. *Future Observations by ngVLA*

In the previous subsection, we show that the protostellar disks of L1527 and IRS 63 have lower spectral indices than the growth front model possibly due to the optically thick emission even though the ring structures of these disks are consistent with the growth front locations. Furthermore, recent ALMA observations suggest that sub-millimeter dust continuum emission may be optically thick in bright ring regions and inner area around protostars in protoplanetary disks (Zhu et al. 2019; Ohashi et al. 2020; Ueda et al. 2020). Therefore, it may be difficult to measure the dust grain size in such regions with ALMA sub-millimeter dust continuum observations. In order to reveal the dust distributions and investigate the growth front, multi wavelengths observations in optically thin regime are needed.

ngVLA will allow us to observe dust grains at midplane of disks with optically thin dust continuum emission because the absorption opacity is much lower in longer wavelength. The absorption opacity at 7 mm wavelength is almost an order of magnitude lower than that at 0.87 mm wavelength. Thus, the optical depth at 7 mm is roughly an order of magnitude lower than that at 0.87 mm.

According to the ngVLA key performance, the entire disks of L1527 and IRS 63 can be imaged at 7 mm wavelength with a spatial resolution of 0.1 arcsec within an integration time of a few minutes for each source. Therefore, ngVLA is an important telescope to reveal the disk structures and investigate the dust grain sizes at the midplane of the disks.

Recent ALMA survey observations with 0.87 mm dust continuum emission have been performed toward various star forming regions (Tobin et al. 2020). These observations also show that some fraction of protostellar disks have substructures such as rings and lopsided structures (Figure 6). It may be possible that the ring structures are explained by the growth front because the ring positions are similar to the growth front locations. To investigate the dust distributions of these disks, observations with longer wavelengths are needed to derive the spectral indices.

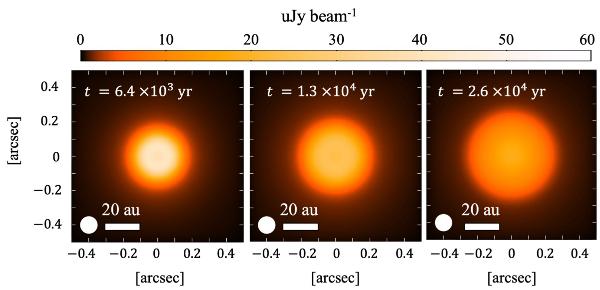

Fig. 7. The intensity maps of the dust coagulation model at $t = 6.4 \times 10^3$ yr, 1.3×10^4 yr, and 2.6×10^4 yr obtained by the radiative transfer calculations with RADMC-3D. The observing wavelength is 7 mm and the spatial resolution is 0.1 arcsec. The distance is 100 pc.

However, these disks are too faint to detect emission of 3 mm or 7 mm wavelength by using current telescopes such as ALMA and VLA. On the other hand, ngVLA will allow us to detect the emission even at 7 mm wavelength above 3σ at ring structures with an integration time of $\lesssim 2$ hrs, thanks to its high sensitivity capability. Even for the MMSN model, the 7 mm dust continuum emission can be imaged with a spatial resolution of 0.1 arcsec with an integration time of ~ 3 hrs. The emission is sharply dropped in the growth front because smaller dust grains emit inefficiently in longer wavelengths, while larger dust grains emit efficiently (Figure 7). Therefore, ngVLA provides us with a great important possibilities to investigate the grain growth not only for bright protostellar disks but also for typical faint protostellar disks.

It should be noted that the collisional fragmentation is ignored in our calculation. By comparing the observed spectral index with the model in detail, we will also further investigate the collisional fragments inside of the growth front.

References

ALMA Partnership, Brogan, C. L., Pérez, L. M., et al. 2015, ApJL, 808, L3

Adachi, I., Hayashi, C., & Nakazawa, K. 1976, Progress of Theoretical Physics, 56, 1756

Andrews, S. M. & Williams, J. P. 2005, ApJ, 631, 1134. doi:10.1086/432712

Andrews, S. M. & Williams, J. P. 2007, ApJ, 671, 1800. doi:10.1086/522885
Andrews, S. M., Huang, J., Pérez, L. M., et al. 2018, ApJL, 869, L41
Brauer, F., Dullemond, C. P., & Henning, T. 2008, A&A, 480, 859
Birnstiel, T., Dullemond, C. P., & Brauer, F. 2010, A&A, 513, A79
Birnstiel, T., Klahr, H., & Ercolano, B. 2012, A&A, 539, A148
Casassus, S., van der Plas, G., M, S. P., et al. 2013, Nature, 493, 191
Dullemond, C. P., Juhasz, A., Pohl, A., et al. 2012, RADMC-3D: A multi-purpose radiative transfer tool, ascl:1202.015
Fedele, D., Tazzari, M., Booth, R., et al. 2018, A&A, 610, A24
Garaud, P. 2007, ApJ, 671, 2091
Garufi, A., Podio, L., Codella, C., et al. 2020, A&A, 636, A65
Hayashi, C. 1981, Progress of Theoretical Physics Supplement, 70, 35
Huang, J., Andrews, S. M., Dullemond, C. P., et al. 2018, ApJL, 869, L42
Isella, A., Guidi, G., Testi, L., et al. 2016, Physical Review Letters, 117, 251101
Kataoka, A., Muto, T., Momose, M., et al. 2015, ApJ, 809, 78
Liu, H. B. 2019, ApJL, 877, L22
Mayor, M. & Queloz, D. 1995, Nature, 378, 355
Nakatani, R., Liu, H. B., Ohashi, S., et al. 2020, ApJL, 895, L2
Ohashi, S., Kataoka, A., van der Marel, N., et al. 2020, ApJ, 900, 81
Ohashi, S., Kobayashi, H., Nakatani, R., et al. 2020, arXiv:2012.04082
Okuzumi, S., Tanaka, H., Kobayashi, H., et al. 2012, ApJ, 752, 106
Sato, T., Okuzumi, S., & Ida, S. 2016, A&A, 589, A15
Sai, J., Ohashi, N., Saigo, K., et al. 2020, ApJ, 893, 51
Segura-Cox, D. M., Schmiedeke, A., Pineda, J. E., et al. 2020, Nature, 586, 228
Sheehan, P. D., & Eisner, J. A. 2017, ApJL, 840, L12
Sheehan, P. D., & Eisner, J. A. 2018, ApJ, 857, 18
Sheehan, P. D., Tobin, J. J., Federman, S., et al. 2020, ApJ, 902, 141
Soon, K.-L., Hanawa, T., Muto, T., et al. 2017, PASJ, 69, 34
Takeuchi, T., & Lin, D. N. C. 2005, ApJ, 623, 482
Takakuwa, S., Saigo, K., Matsumoto, T., et al. 2017, ApJ, 837, 86
Tanaka, H., Himeno, Y., & Ida, S. 2005, ApJ, 625, 414
Tsukagoshi, T., Muto, T., Nomura, H., et al. 2019, ApJL, 878, L8
Tobin, J. J., Sheehan, P. D., Megeath, S. T., et al. 2020, ApJ, 890, 130
Ueda, T., Kataoka, A., & Tsukagoshi, T. 2020, ApJ, 893, 125
van der Marel, N., van Dishoeck, E. F., Bruderer, S., et al. 2013, Science, 340, 1199
Weidenschilling, S. J. 1977, MNRAS, 180, 57
Williams, J. P. & Cieza, L. A. 2011, ARA&A, 49, 67
Zhu, Z., Zhang, S., Jiang, Y.-F., et al. 2019, ApJL, 877, L18